MEMS Navigation-Grade Electro-Optical Accelerometer

Dr. Richard L. Waters[†] and Dr. Thomas E. Jones[††]
Space & Naval Warfare Systems Center, San Diego
53560 Hull Street
San Diego, CA 92152-5001
USA

[†]Code 2876, Advanced Integrated Circuits and Sensors
[††]Code 2315, Navigation and Applied Sciences Department

richard.waters@navy.mil / joneste@spawar.navy.mil

ABSTRACT

Accurately measuring displacement of mechanical components on micro-scale devices is often the limiting factor affecting resolution for many MEMS-based sensors including accelerometers, Coriolis-based gyroscopes, pressure sensors, temperature sensors, and magnetometers. This paper introduces a novel electro-optical displacement detection scheme which has been applied to navigation-grade MEMS accelerometers under funding from the Office of Naval Research (ONR). The optical detection method is extremely sensitive to displacements, and generates large steady-state currents thereby eliminating the necessity to co-integrate sensitive amplification electronics next to the sensing element. Experimental measurements have resulted in a 10 femtometer noise floor without the need to co-integrate amplifying control electronics within the same package as the accelerometer sensor. This technique is based on the monolithic integration of a Fabry-Perot optical interferometer and a photodiode.

1.0 INTRODUCTION

High sensitivity accelerometers are critical for the next generation navigation and guidance systems including tight coupling to existing GPS engines, pressure sensors, and platform stabilization for space applications. The impetus for a MEMS-based inertial accelerometer is based upon the hopes of realizing a low cost, small, lightweight and highly sensitive alternative to existing macro-scale approaches. The successful fabrication of a low cost, high-sensitivity MEMS accelerometer will result in new applications for both consumer and military users that aren't feasible with current technologies. Examples include personal hand held navigators for military and consumer applications, as well as GPS-denied navigation applications such as in valleys, urban areas, and within buildings and caves.

Numerous MEMS devices used for the detection of motion, position, pressure, and temperature rely upon the precise measurement of the displacement of a proof mass attached to a spring. To detect these displacements several techniques have been employed including measurement of charge on a variable capacitor [1-4], change in optical transmission through a Bragg grating [5], change in resistance of a piezoresistor [6-9], and more recently measurement of tunneling current through a well-controlled airgap [10-13]. Of these techniques, tunneling displacement sensors hold the best promise for realizing small, highly sensitive transducers required for navigation and acoustic applications. Tunneling transducers take advantage of the exponential sensitivity in tunneling current to the tunneling gap distance in order to realize appreciable changes in current with input acceleration. Typical steady state tunneling current is

Waters, R.L.; Jones, T.E. (2007) MEMS Navigation-Grade Electro-Optical Accelerometer. In *Military Capabilities Enabled by Advances in Navigation Sensors* (pp. 12-1 – 12-16). Meeting Proceedings RTO-MP-SET-104, Paper 12. Neuilly-sur-Seine, France: RTO. Available from: http://www.rto.nato.int.

approximately 1-2 nA [14]. In order to achieve this steady-state current, an airgap on the order of approximately 10 Å (1.0 nm) must be maintained via force rebalancing. Due to the limited tunneling area (one metal atom on the surface of each side of the airgap), larger tunneling currents are difficult to obtain. In addition, tunneling transducers may have high temperature-sensitivity since thermal expansion coefficient mismatches can alter the tunneling gap distance [15]. Finally, tunneling accelerometers are reported to have a significant 1/f (flicker) noise contribution and a high variability in the tunneling barrier height [16].

Capacitive-based accelerometers have been the most widely developed and commercialized due to the operational simplicity of the device and available fabrication methods. Obtaining high resolution, high stability capacitive accelerometers, however, has been difficult due to the low steady-state capacitances and the tight processing tolerances. To increase the sensitivity of these capacitive accelerometers, the size and surface area of the devices are generally increased, sense gaps decreased to a micron or less, and the quality factor, Q, increased. All of these factors make high resolution, high stability capacitive sensors difficult to realize.

We present a novel optical transducer concept for the precise measurement of a proof mass attached to a spring that has raw sensitivity greater than that of a tunneling transducer and stability exceeding those of current capacitive accelerometers. The concept involves the integration of a Fabry-Perot interferometer and a photodiode on a (100) Si substrate using surface and / or bulk micro-machining techniques resulting in a compact device with minimal parasitic elements. MEMS-based Fabry-Perot Interferometers have recently been investigated for use in numerous applications including chemical sensing [17], Wavelength Division Multiplexed (WDM) optical communications [18], and pressure sensors [19]. The monolithic integration of a Fabry-Perot interferometer and a p-n photodiode on a (111) silicon substrate has been reported elsewhere for use as a versatile switch and amplifier [20].

2.0 CONCEPTUAL THEORY

A Fabry-Perot cavity is extremely sensitive to changes in the effective cavity length. A Fabry-Perot cavity first devised by C. Fabry and H. Perot in 1899 utilizes multiple beam interference. In the field of optics, it is usually used to measure wavelengths of light with high precision and study the fine structure of spectral lines. In its simplest form, a Fabry-Perot cavity consists of two optically flat, partially transmissive and parallel mirrors separated by a distance, y. In the accelerometer application, that distance is designed to be a function of the acceleration, a. In such a case where one of the mirrors is allowed to move, the structure is referred to as an interferometer. The two mirrors form an optically resonant cavity whereby the transmission of monochromatic light through the cavity can be made to be highly sensitive to displacement of one mirror with reference to the second fixed mirror. For an ideal Fabry-Perot cavity, the two reflecting surfaces are separated by a medium (generally air) with thickness, y(a), refractive index, n, and absorption coefficient, α. The ideal Fabry-Perot cavity is illustrated in Figure 1 below. Assuming a symmetric structure ($r_{01} = -r_{12}$ and $t_{01} = t_{12}$) with no absorption within the mirrors or the cavity at the wavelength of interest, an analytical expression for the photo-generated current as a function of the effective airgap displacement, y(a), can be obtained as

$$I_{ph} = \Re P_{in} \frac{1}{1 + F\ U^2} \tag{1}$$

$$U = \sin\left(\frac{2\pi}{\lambda}\left(n_1 y(a)\right)\right) \tag{2}$$

In equations (1-2), F is the Finesse of the cavity, P_{in} is the input optical power incident normal to the surface of the upper mirror, $\Re$ is the responsivity of the photodiode in amperes/watt (A/W), and λ is the wavelength of the incident light. In equations (1-2) it is assumed that the mirrors are lossless and absorption occurs only in the medium between the mirrors.

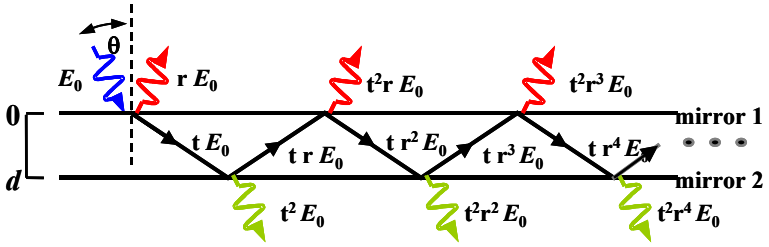

Figure 1. Fabry-Perot Interferometer comprised of two optically flat and parallel mirrors.

Figure 2a is a plot of the relative transmission intensity through the Fabry-Perot interferometer as a function of the spacing between the mirrors. Figure 2b is a plot of the relative transmission of the Fabry-Perot cavity for various mirror qualities. The plot was generated using three different values of mirror reflectivity, R=0.2, R=0.5, and R=0.9, corresponding to a Finesse of 1, 8, and 360, respectively. The Finesse is a figure of merit for a Fabry-Perot cavity and is a measure of the wavelength selectivity when used as a filter, or displacement sensitivity when used as an inertial system with a fixed monochromatic source. It is clear in Fig. 2a and 2b that small displacements result in large changes in relative transmission of light through the cavity, particularly for large values of Finesse. The general operation of the device is depicted in Figure 3 where the mirror cavity spacing is optimized to reside along the maximum slope. A small perturbing force about the nominal operating point results in a large differential output current.

For the more general case, the structure may not be symmetric, $r_{01} \neq -r_{12}$ and $t_{01} \neq t_{12}$, the mirrors may be comprised of any number of arbitrary dielectric or metallic layers, and absorption may exist anywhere within the structure. In this instance, a characteristic matrix similar to that obtained for transmission line structures needs to be solved for each layer. For further information on the solution of an arbitrary dielectric stack the reader is referred to *Principles of Optics* by Born and Wolf [21].

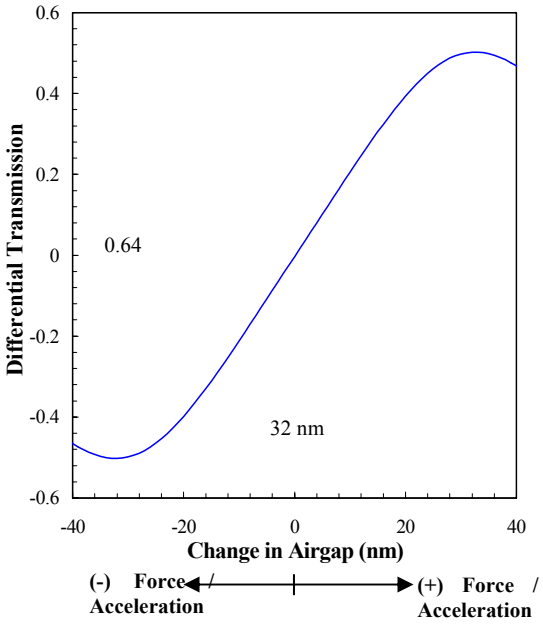

Figure 2a. Change in transmission with a variable airgap. The nominal airgap position is taken to be at the maximum slope.

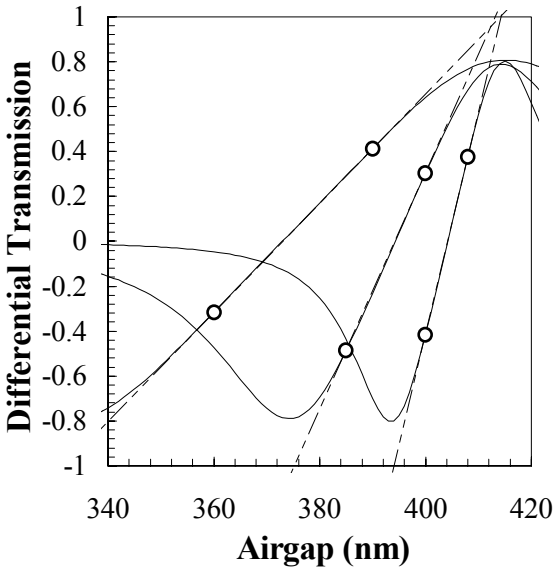

Figure 2b. Change in transmission for cavities with increasing mirror reflectivities.

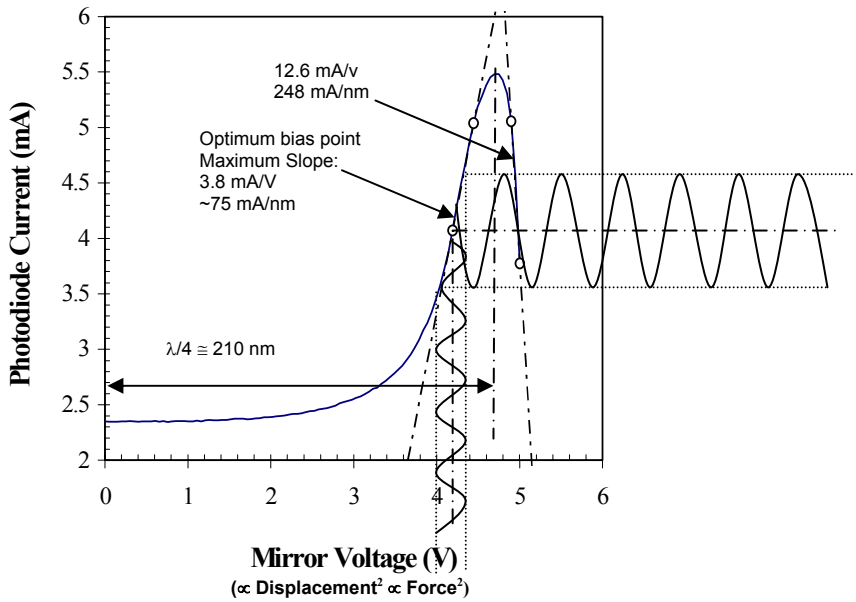

Figure 3. Operation of the transduction technique about the nominal operating point. Small perturbations about the nominal operating point are converted to a photodiode current via the optical Fabry-Perot transduction mechanism.

In the absence of absorption, and in a resonant condition, the transmission of light through the optical cavity is equal to unity even when the upper mirror itself has a finite reflectivity. This is contrary to what one might expect since it seems reasonable to assume that if the upper mirror has a reflectivity of 0.9, then 90% of the incident light should be lost and not transmitted through the resonant cavity. However, light that is transmitted through the upper mirror and then reflected off the lower mirror is exactly anti-phase with the incident light being reflected from the upper mirror, thereby nulling the reflected signal.

By substituting equation (2) into equation (1) and taking the derivative of current, I_{ph}, with respect to acceleration, a, an approximate analytical expression for the current sensitivity is obtained as

$$\frac{dI_{ph}}{da} = -\Re P_{in} \frac{m}{k} \frac{2FUV}{(1+FU^2)^2} \tag{3}$$

$$V = \cos\left(\frac{2\pi}{\lambda}\left(n_1 y(a)\right)\right) \tag{4}$$

Rewriting equation (3-4) in terms of the photo-generated current a more tractable expression is obtained as

$$\frac{dI_{ph}}{da} \propto \frac{P_{in}^2 F}{\Re P_{in} \omega_0^2} \tag{5}$$

From equations (3-5), it is clear that in order to increase the sensitivity of the device any one of the following fabrication / operational changes can be made: 1) Increasing the inertial mass, 2) decreasing the spring constant, 3) increasing the reflectivity of the mirrors thus increasing the Finesse, or by 4) increasing the input optical power to the photodiode. Methods 1) and 2) for increasing the sensitivity are equivalent to lowering the resonant frequency, ω_o, of the inertial mass. Figure 4 is a plot of the Finesse as a function of the number of dielectric stacks that comprise the layers of the mirror. From the figure, it can be seen that for approximately every three consecutive dielectric stacks deposited, the sensitivity, as given by equation (5), increases an order of magnitude.

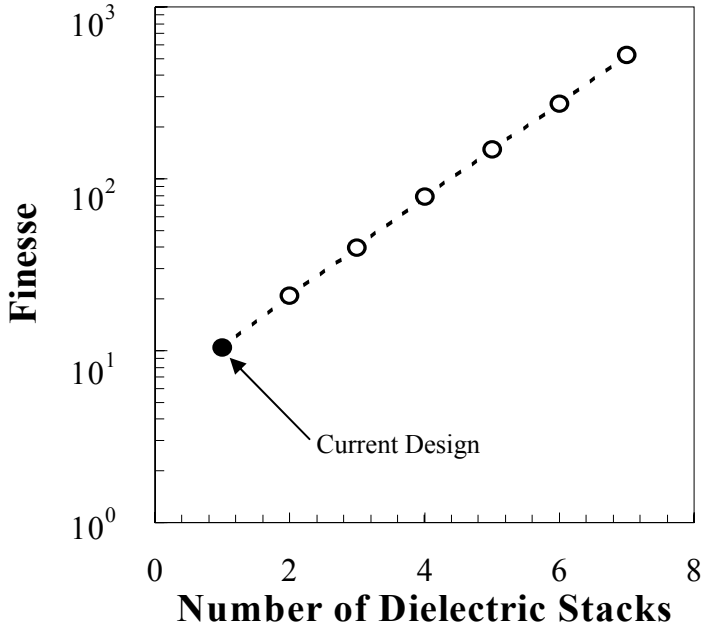

Figure 4. Change in calculated Finesse, a function of the reflectivity of the mirrors, as a function of the number of deposited dielectric stacks. The black dot represents the expected Finesse from the design currently under fabrication.

3.0 DEVICE STRUCTURE

Two generations of electro-optical accelerometers have been fabricated to date with a third generation currently in process. The first generation was a surface micro-machined approach aimed at demonstrating the concept of monolithically integrating a Fabry-Perot cavity with a silicon photodiode. The second and third generations are a combination of bulk and surface micromachining, whereby the dielectric mirror developed during the first generation was applied to a suspended silicon mass.

Both first and second generation devices were fabricated at the Space and Naval Warfare Systems Center San Diego's Integrated Circuit Fabrication Facility. Phosphor doped (100) bulk silicon with a sheet resistance of ρ = 10-30 Ω-cm serves as the starting material. Boron implantation is performed to form a shallow one-sided junction so as to collect as much transmitted light into the depletion region of the photodiode as possible, thus increasing the responsivity (A/W). A series of well-controlled silicon dioxide and silicon nitride depositions in combination with dry/wet etching is used to form the final structure. A thin semitransparent conductive layer is incorporated into the upper mirror so as to allow for electrostatic control of the airgap spacing between the upper and lower mirrors. The sacrificial layer, in this instance, is approximately 0.8 μm of undoped polysilicon that is later removed using a highly selective Tetra-Methyl Ammonium Hydroxide (TMAH) etch. Figure 5 is a cross-sectional view of an example MEMS USA sensor.

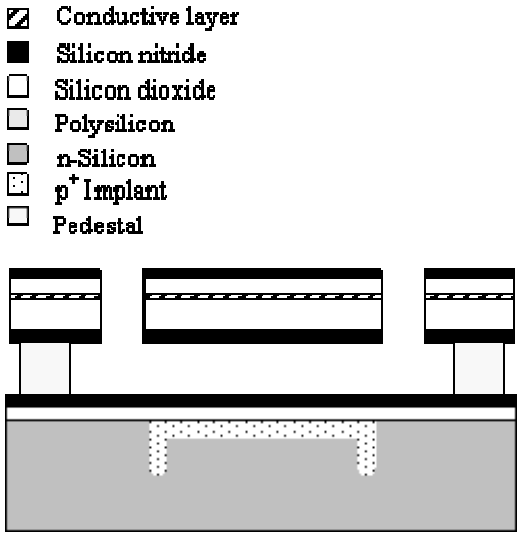

Figure 5. Cross-sectional drawing of an example MEMS electro-optical sensor.

Figure 6a – 6d below, are micrographs of fabricated first generation sensors. The upper mirror in Figure 6a is the 50 micron diameter circular disk suspended by the springs while the lower mirror is deposited on the surface of the entirety of the silicon substrate. Upper and lower mirrors are separated by an airgap of distance equal to the thickness of the sacrificial poly-silicon. Aligned directly beneath the upper mirror is an implanted one sided photodiode junction. Figure 6b is an SEM micrograph detailing the structure of the dielectric mirror stack comprising the upper mirror and springs. Figure 6c is an alternative spring design to the design shown in Figure 6a. Figure 6d shows an array of first generation sensors on a single silicon die. In this case the optical field of view from the microscope limited the photograph to an area of 1 mm X 1.5 mm which contains a total of 12 sensors. Each of the sensors in the array can be tailored to have different spring designs and hence different resonant frequencies.

Second generation sensors were fabricated using a combination of surface and bulk micro-machining. The second generation sensors were designed with the goal of further increasing sensitivity of the device by increasing the mass of the structure and increasing the long-term stability and robustness. The later was accomplished by incorporating dual crystalline silicon springs that attached to both the upper and lower edges of the silicon proof mass. The same dielectric mirror stack used in the first generation design was also incorporated onto the bottom of the silicon proof mass in the second generation design. A Deep Reactive Ion Etch (DRIE) was used to etch the geometry of the springs as well as create an optical light valve for the passage of the source laser light to the upper mirror. A second wafer containing the lower mirror and the implanted photodiode was also fabricated and subsequently bonded to the proof mass wafer. The second generation fabrication process also named the “Universal MEMS Integrated Dual-Spring” or UMIDS process allows for not only optical resonant cavities but also other optical devices such as optical shutters and diffractive gratings as well as traditional capacitive devices including comb-drives and resonator structures. Any of these structures can be made in any combination using the UMIDS process to create various sensor types including 1-axis, 2-axis, and 3-axis accelerometers, as well as gyroscopes and pressure sensors.

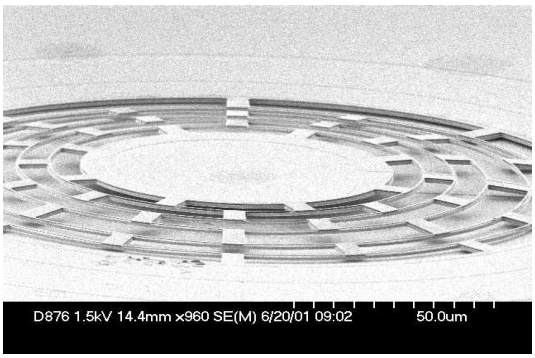

Figure 6a. SEM micrograph of a first generation Fabry-Perot Proof-of-Concept accelerometer.

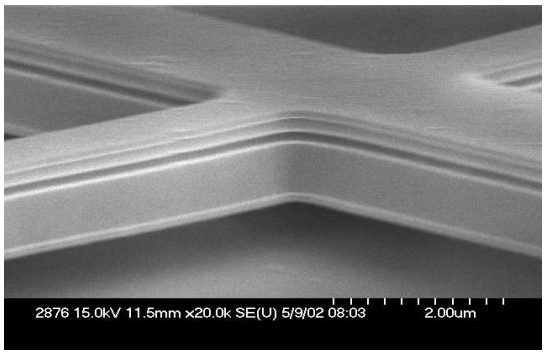

Figure 6b. SEM micrograph of the dielectric mirror stacks comprising both the upper mirror and spring structures.

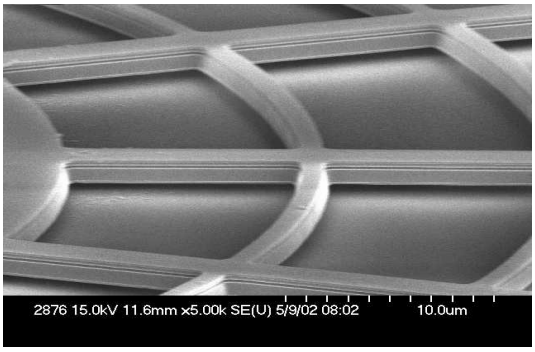

Figure 6c. Alternative spring configuration

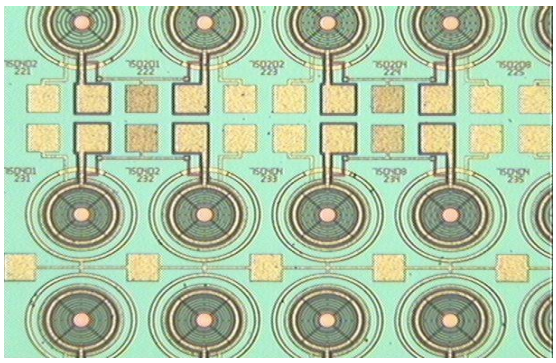

Figure 6d. Optical micrograph of a 3x4 array of first generation sensors. The field of view is 1 mm X 1.5 mm.

Figure 7 is a cross-sectional drawing of an example second generation device. The figure shows the final bonded configuration of the proof mass wafer containing the upper mirror to the lower mirror wafer containing the implanted photodiode. The lower wafer also contains control electrodes for electrostatically controlling and maintaining the optimum position of the Fabry-Perot airgap formed by the separation between the upper and lower mirrors.

Figure 8a-8c are optical micrographs of completed second generation sensors. Figure 8a shows an array of sensors on a 6 inch (150 mm) diameter silicon wafer. The wafer contains over 1000 sensors with over 20 unique designs. Figure 8c is an optical micrograph of an individual second generation sensor. The image shows the proof mass with crystalline silicon springs attached to a lower mirror wafer containing wire bond pads and control electrodes directly beneath the proof mass.

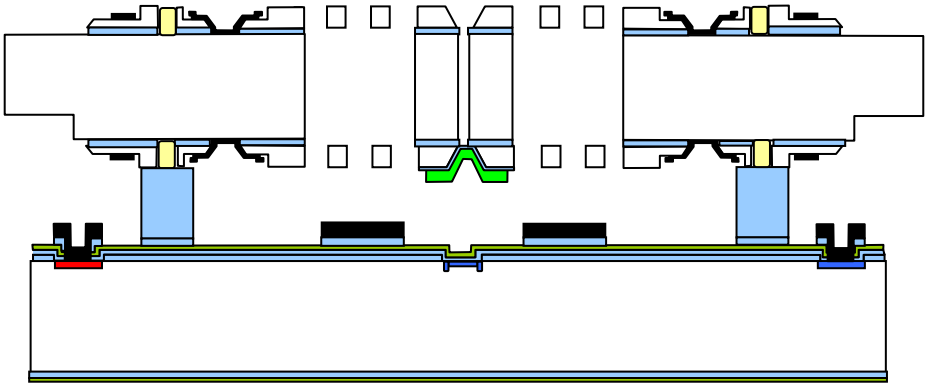

Figure 7. Cross-sectional drawing of a second generation sensor fabricated using the UMIDS fabrication process.

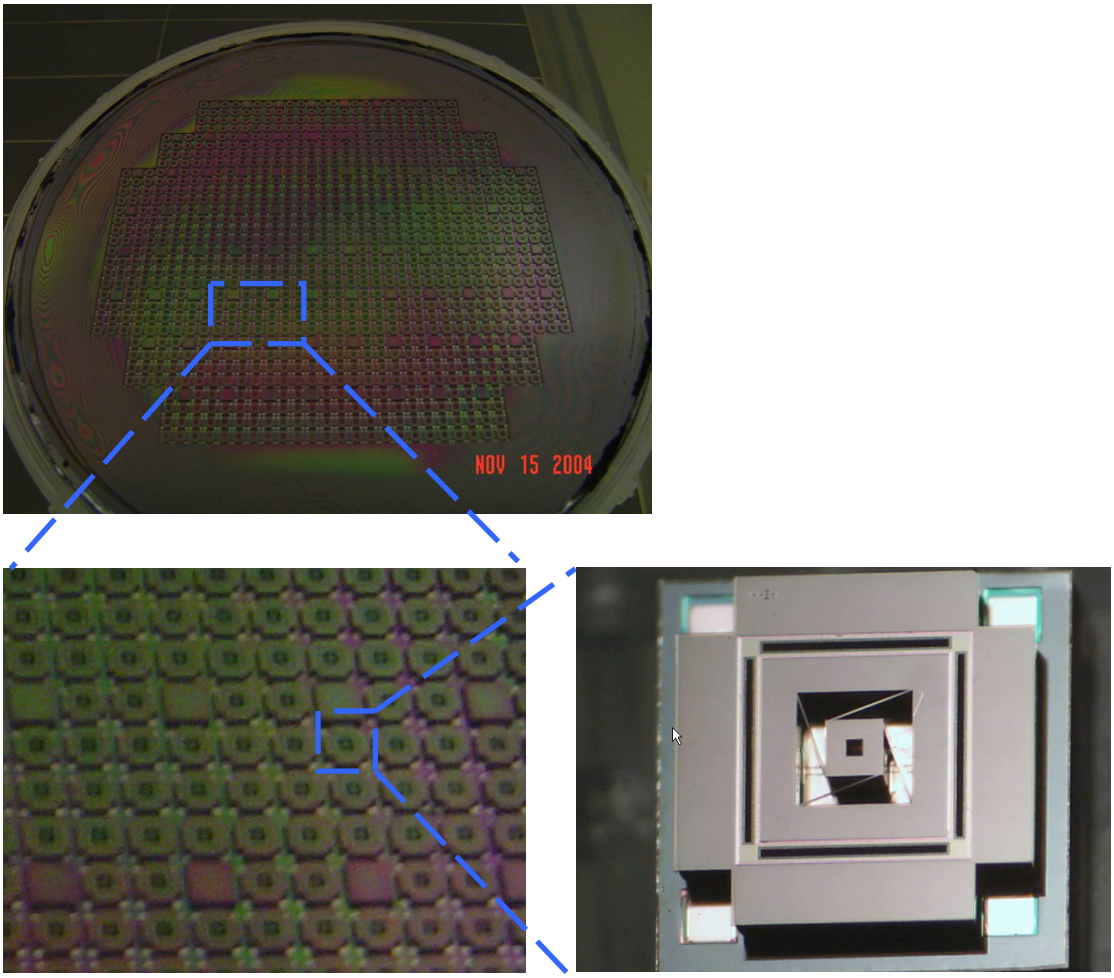

Figure 8a-8c. Fully fabricated second generation sensor using a combination of surface and bulk micro-machining.

4.0 DEVICE PACKAGING

Preliminary packages for characterization and evaluation were fabricated using discrete alumina components and commercially available flanged TO-8 headers and caps. The package incorporates the MEMS sensor, an optically aligned Vertical Cavity Surface Emitting Laser (VCSEL), thermistor for monitoring temperature, monitor photodiode, and a thermoelectric cooler (TEC) for maintaining the temperature of the laser source and MEMS component. Figure 9a-9c illustrates the assembly sequence. Figure 9a shows the MEMS die attached to an alumina substrate patterned with gold with die attach and wire bond areas. A thermistor is attached to the alumina substrate, and two alumina spacers with gold are attached on either side of the MEMS die. As can be seen in Figure 9b, the alumina spacers are used to attach an alumina bridge directly over the MEMS die. The bottom side of the alumina substrate contains a VCSEL laser source measuring 200 µm X 200 µm X 150 µm thick. The VCSEL is optically aligned to the small opening in the middle of the proof mass shown in Figure 9a. The assembly of Figure 9b is then mounted on top of a TEC and attached to a flanged TO-8 header. Finally, a lid is seam-sealed onto the header to complete the assembly process.

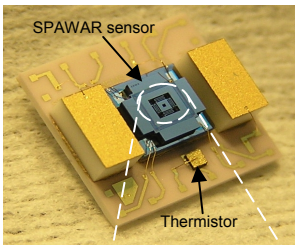

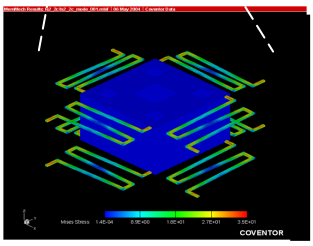

Figure 9a. Attachment of a second generation sensor onto an alumina substrate patterned with gold.

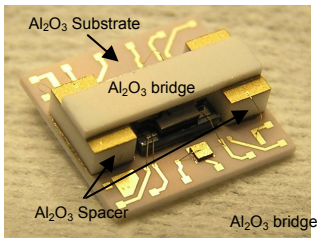

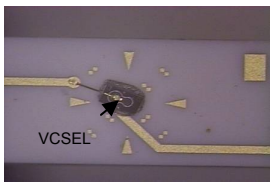

Figure 9b. An alumina bridge containing the laser source is attached across the spacers and aligned to the MEMS device on the substrate.

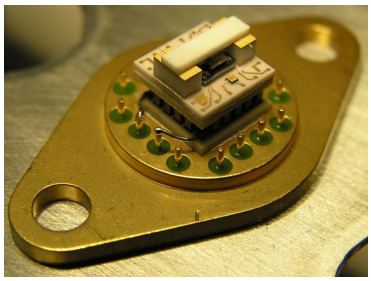

Figure 9c. The complete assembly is attached onto a TO-8 header.

A second more optimized and commercially viable package was developed based on the preliminary package design described above. The new package extended the spacer concept to include a complete ring around the perimeter of the alumina substrate. The bridge developed in the preliminary package became a lid with hermetic seal ring and the electrical I/O was made via a 28-pin lead-frame attached directly under the alumina substrate. In order to better facilitate thermal management of the laser source, the entire assembly was flipped upside down, i.e. the VCSEL was mounted on the substrate while the MEMS die was attached to the underside of the alumina lid as shown in Figure 10a. Figure 10b is a photo of the alumna substrate with integrated spacer ring and electrical I/O. Figure 10c is a photo of the alumina lid containing the MEMS die attach area and hermetic seal ring while Figure 10d is a completed assembly.

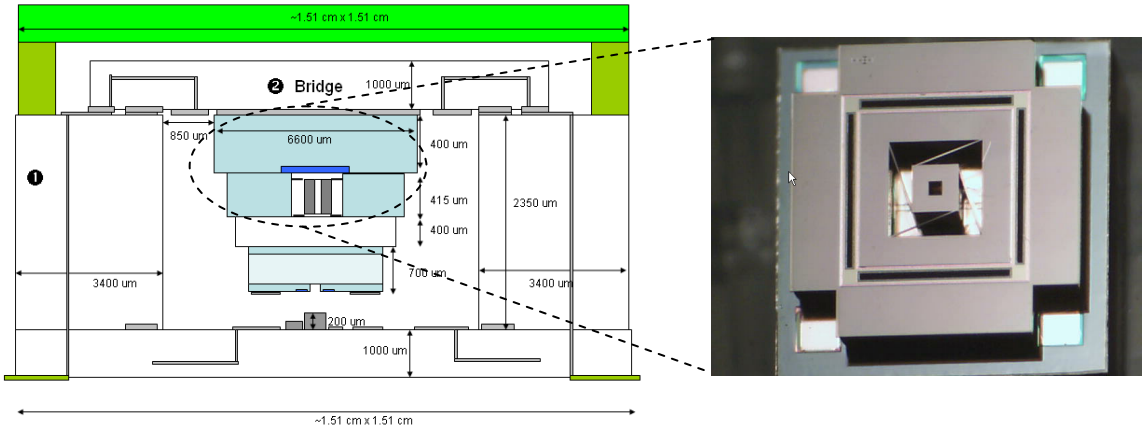

Figure 10a. Cross-sectional drawing of the optimized package showing the laser attach on the substrate while the MEMS sensor die is attached to the lid.

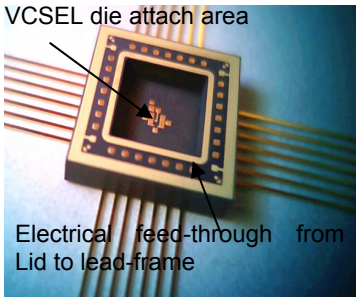

Figure 10b. Alumina substrate laser attach area and lead-frame I/O.

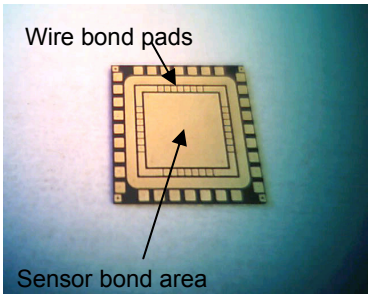

Figure 10c. Alumina lid with MEMS die attach area and hermetic seal ring

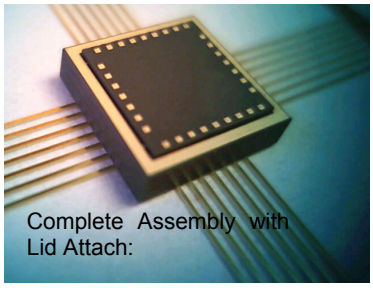

Figure 10d. Completed assembly.

5.0 EXPERIMENTAL RESULTS

All experimental measurements were obtained using a Labworks vibration table along with an LDS-Dactron shaker control system and 24-bit ADC. Where applicable, a Dytran 3055B3 reference accelerometer with an acceleration bias stability of 1 mg was used to control shaker table amplitude and frequency.[1]

Preliminary open-loop results were obtained by driving the laser with a constant current source and biasing the mirror electrodes such that the airgap was positioned to coincide with the maximum slope efficiency of the transducer. The proof mass was operated open-loop implying that no feedback voltage was used to force-rebalance the mass thus limiting the maximum upper acceleration limit of the device. Figure 11 shows the output of both the Dytran reference accelerometer and the MEMS electro-optical accelerometer when vibrated a frequency of 100 Hz and an acceleration of 10 mg (≅ 10 gal). The 10 mg acceleration amplitude was measured directly by the Dytran accelerometer while the MEMS sensor measured a voltage output of 1.25 V using a 10 KΩ transimpedance amplifier. The result is a measured scale factor of 125 V/g for this particular MEMS accelerometer. This is consistent with a transduction of

[1] Note on acceleration units: In measuring units of acceleration, it is common practice in the field to use 'g' to represent one standard unit of nominal earth-gravity acceleration (980 cm/s^2). The metric unit of acceleration is the gal, named after Galileo, where 1 gal = 1 cm/s^2 by definition. Thus, 1 mg = 0.98 cm/s^2 = 9.8x10^{-3} m/s^2 ≅ 1 gal; also, 1 μg ≅ 1 mgal.

62.5 μA/nm of proof mass displacement. To date, transduction values as large as 75 μA/nm have been measured. Figure 12 is a plot of another electro-optical MEMS device with a 20 V/g scale factor operated at an acceleration amplitude of 150 mg (≅ 150 gal). In this instance, because the proof mass is operated open-loop, both minimum and maximum voltages have a dip in what would otherwise be a 100 Hz sinusoidal curve. The dip is due to the fact that the displacement of the proof mass under an acceleration amplitude of 150 mg is sufficient cause the device to temporarily operate beyond either the minimum or maximum transmission values shown in Figure 3.

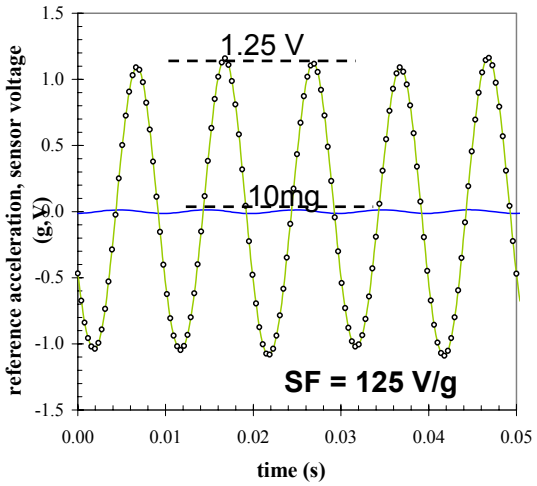

Figure 11. Measured open-loop response of MEMS optical accelerometer (green curve) and reference Dytran accelerometer (blue curve) when operated at 100 Hz and an acceleration amplitude of 10 mg (≅ 10 gal).

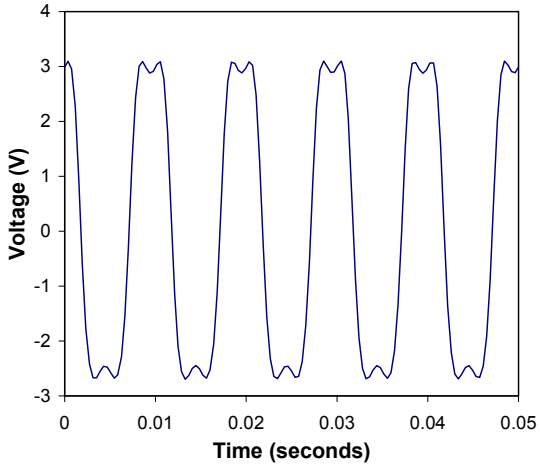

Figure 12. Open-loop response of a 20 V/g MEMS optical accelerometer when operated at an acceleration amplitude of 150 mg (≅ 150 gal).

A large scale factor directly impacts the equivalent acceleration noise output for a measured voltage noise output. Figure 13 is a plot of the Power Spectral Density (PSD) of the MEMS electro-optical accelerometer for scale factors of 3 V/g and 125 V/g respectively. The voltage noise source is limited to the noise inherent in the optics, namely laser Relative Intensity Noise (RIN) and photodiode shot noise. A larger scale factor clearly lowers the acceleration noise floor for a fixed system voltage noise source by an amount proportional to the scale factor. Also shown in Figure 13, for comparative purposes, is a Colibrys SF1500S seismic sensor. The SF1500S was operated single-ended since the differential output was not working on this particular accelerometer during the writing of this paper. It is anticipated that proper operation of the SF1500S in differential mode would decrease the measured PSD noise floor to approximately 300-500 nm/√Hz as given in the SF1500S data sheet.

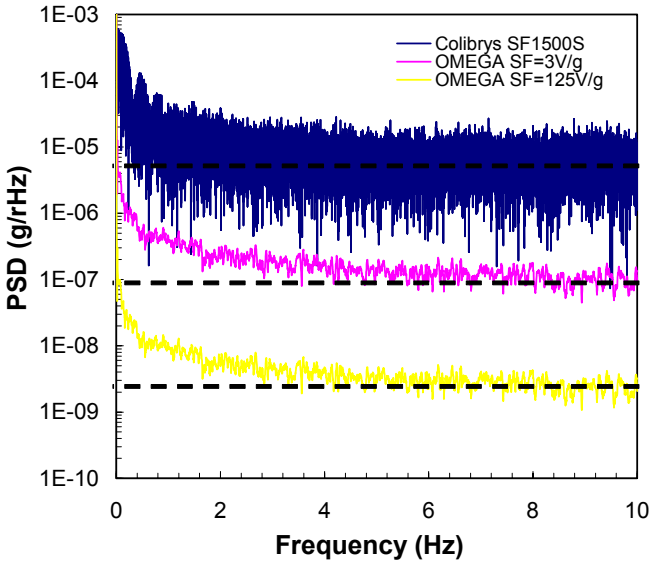

Figure 13. PSD data for the MEMS electro-optical accelerometer with scale factor of 3 V/g and 125 V/g. For comparative purposes, Colibrys SF1500S accelerometer is shown measured with a single ended output.

Digital closed-loop electronics were designed to operate the laser in constant power using a monitor photodiode integrated into the packages previously shown in Figures 9-10. Direct measurement of the monitor photodiode output current was digitally sampled and used to adjust the laser drive current. The ability to accurately close the loop around the laser source provides the sensor with a very good long-term power and hence bias stability. Wavelength drift of the laser source is another concern potentially affecting long-term stability of the sensor system. Wavelength of the laser is most acutely affected by changes in operating temperature. To address this issue a digital loop closure around the thermistor and TEC was made. Temperature stability of less than 0.01 degree Celsius was achieved resulting in a wavelength fluctuation of 1 pm (10^{-12} meters) based on a temperature sensitivity of 0.1 nm/ºC for the VCSEL source. In addition, long-term testing of the laser sources indicates that the wavelength drifts less than 4 ppm per day when operated using closed-loop electronics.

Figure 14 is a plot of the Allan Deviation for the electro-optical sensor when operated with closed-loop electronics. The Allan Deviation gives the standard deviation of the output voltage versus integration time and is useful for looking at long-term drift of sensor systems [22]. Typically, for short integration times, the standard deviation decreases as the integration time increases since more noise is being averaged (integrated) out during the sampling period. At some point, however, no further reduction is noise floor can be achieved no matter how long the integration time. Eventually, for very long integration times, the noise floor begins to increase again due to long-term drifting of the sensor and uncorrelated noise sources. Two plots are shown in Figure 14. The first is a plot of the Allan Deviation of the monitor photodiode and the second is a plot of the sensor photodiode output. The monitor photodiode has very good long-term stability since the loop-closure around the laser forces the monitor photodiode to have a very constant long-term output. The sensor photodiode closely follows the monitor photodiode output initially, but eventually diverges due to uncorrelated noise in the sensor and monitor diodes. However, even though the standard deviation of the sensor photodiode output has increased to 0.065 mV after 1000 seconds of

integration, the equivalent acceleration deviation and hence acceleration stability is less than 10 μg (≅ 10 mgal) when a scale factor of 10 V/g is used.

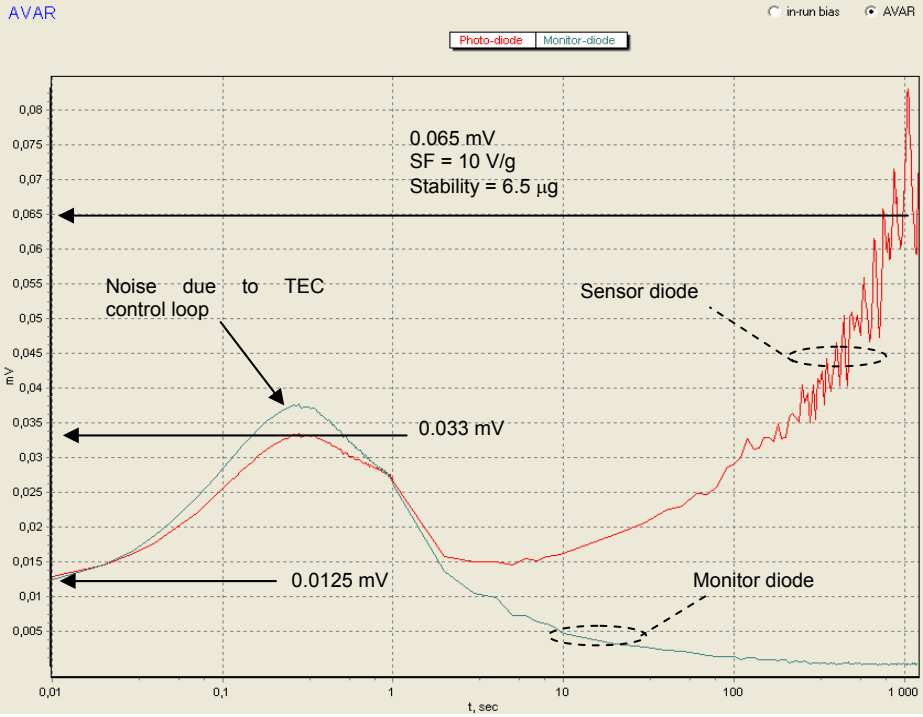

Figure 14. Allan Deviation plot of both the monitor and sensor photodiodes. Loop closure is performed around the monitor photodiode, hence the very good ling-term stability. Although the sensor diode output begins to deviate form the monitor, the equivalent standard deviation in acceleration after 1000 seconds of integration is less than 10 μg (≅ 10 mgal).

6.0 CONCLUSIONS

We have presented a novel optical MEMS-based transducer for the precise measurement of displacement of a proof mass. The concept was shown to have a large scale factor (125 V/g) due to measured transduction values as large as 75 μA/nm. Very good long-term stability was also demonstrated with acceleration instabilities below 10 μg with a 10 V/g scale factor for integration times up to 1000 seconds. A novel fabrication process was also introduced that incorporates dual-crystalline silicon springs for increased mechanical stability and with sufficient flexibility to fabricate optical and capacitive devices simultaneously. The same electro-optical transduction concept along with fabrication process can be extended to multi-axial accelerometers, gyroscopes and pressure sensors.

7.0 ACKNOWLEDGEMENTS

The authors would like to thank the In-House Independent Research (ILIR) Program at the Space and Naval Warfare Systems Center San Diego for supporting the initial foundation work for this accelerometer concept, and the Office of Naval Research (ONR), Dr. John Kim, Code 313, for supporting the development and demonstration of a prototype accelerometer under the ONR Navigation Program.

8.0 REFERENCES

[1] N. Yazdi, K. Najafi, “An All-Silicon Single-Wafer Micro-g Accelerometer with a Combined Surface and Bulk Micromachining Process”, J. Microelectromechanical Systems, Vol. 9., No. 4, Dec. 2000, p.544-550.

[2] J. Bernstein, R. Miller, W. Kelley, P. Ward, “Low-Noise MEMS Vibration Sensor for Geophysical Applications”, J. Microelectromechanical Systems, Vol. 8, No. 4, Dec. 1999, p.433-438.

[3] K.H. Chau, S.R. Lewis, Y. Zhao, R.T. Howe, S.F. Bart, R.G. Marcheselli, “An Integrated Force-Balanced Capacitive Accelerometer for Low-G Applications”, Transducers ’95, June 25-29, 1995, p. 593-596.

[4] J. W. Weigold, K. Najafi, S.W. Pang, “Design and Fabrication of Submicrometer, Single Crystal Si Accelerometer”, J. Microelectromechanical Systems, Vol. 10, No. 4, Dec, 2001, p.518-524.

[5] T. Storgaard-Larsen, S. Bouwstra, O. Leistiko, “Opto-Mechanical Accelerometer Based on Strain Sensing by a Bragg Grating in a Planar Waveguide”, Transducers ’95, June 25-29, 1995, p.667-670.

[6] D.L. Devoe, A.P. Pisano, "Surface Micromachined Piezoelectric Accelerometers (PiXLs)", J. Microelectromechanical Systems, Vol. 10, No. 2, June 2001, p.180-186.

[7] H. Chen, M. Bao, H. Zhu, S. Shen, "A Piezoresistive Accelerometer with Novel Vertical Beam Structure", Transducers '97, June 16-19, 1997, p.1201-1204.

[8] D.L. Devoe, A.P. Pisano, "A Fully Surface-Micromachined Piezoelectric Accelerometer", Transducers '97, June 16-19, 1997, p.1205-1208.

[9] B. Puers, L. Reynaert, W. Snoeys, W.M. Sansen, "A New Uniaxial Accelerometer in Silicon Based on the Piezojunction Effect", IEEE Trans. On Elec. Dev., Vol. 35, No. 6., June 1988, p.764-770.

[10] C.H. Liu, T.W. Kenny, “A High Precision, Wide-Bandwidth Micromachined Tunneling Accelerometer”, J. MicroElectromechanical Systems, Vol. 10, no. 3, Sept. 2001, p. 425-433.

[11] C. Yeh, K. Najafi, “CMOS Interface Circuitry for a Low-Voltage Micromachined Tunneling Accelerometer”, J. Microelectromechanical Systems, Vol. 7, No. 1, March 1998, p. 6-15.

[12] C. Yeh, K. Najafi, “A Low-Voltage Tunneling-Based Silicon Microaccelerometer”, IEEE Transactions on Electron Devices, Vol. 44, No. 11, p. 1875-1882, November 1997.

[13] J. Grade, A. Barzilai, J.K. Reynolds, C.H. Liu, A. Partridge, L.M. Miller, J.A. Podosek, T. Kenny, “Low Frequency Drift in Tunnel Sensors”, 1997 International Conference on Solid-State Sensors and Actuators, Transducers ’97, p. 871-874, June 16, 1997.

[14] T.W. Kenny, S.B. Waltman, J.K. Reynolds, and W.J. Kaiser, “Micromachined silicon tunnel sensor for motion detection”, Appl. Phys. Lett., Vol. 58, No. 1, p.100, Jan. 1991.

[15] C.H. Liu, A.M. Barzilai, J.K. Reynolds, A. Partridge, T.W. Kenny, J.D. Grade, H.K. Rockstad, “Characterization of a High-Sensitivity Micromachined Tunneling Accelerometer with Micro-g Resolution”, J. Microelectromechanical Systems, Vol. 7, No. 2, June 1998, p. 235-244.

[16] N. Yazdi, F. Ayazi, K. Najafi, "Micromachined Inertial Sensors", Proceedings of the IEEE, Vol. 86, No. 8, Aug. 1998, p.1640-1659.

[17] J. Han, D.P. Neikirk, M. Clevenger, J.T. McDevitt, “Fabrication and Characterization of a Fabry-Perot Based Chemical Sensor, “Proceedings of the SPIE, Vol. 2881, 1996, p.171-178.

[18] M. Frank Chang, M.C. Wu, “Surface Micromachined Devices for Microwave and Photonic Applications”, Proceedings of the SPIE, Vol. 3419, 1998, p.214-226.

[19] M.G. Kim, J. Park, S.W. Kang, B.K. Sohn, “A Fiber Optic Fabry-Perot Pressure Sensor with the Si3N4/SiO2/Si3N4 diaphragm Fabricated using Micromachining Technology”, Proceedings of the SPIE, Vol. 3242, 1997, p347-353.

[20] R. Waters, J. Patterson, B. Van Zeghbroeck, “Micromechanical Optoelectronic Switch and Amplifier (MIMOSA)”, IEEE J. of Selected topics in Quantum Electronics, vol 5, no. 1, pp. 33-35, JAN/FEB 1999.

[21] Max Born, Emil Wolf, Principles of Optics, Pergamon Press, Oxford England, 1980.

[22] D.W. Allan, "The Statistics of Atomic Frequency Standards", *Proc. IEEE*, Vol. 54, No. 2, pp. 221-230, Feb. 1966.